

3D fictitious wave domain CSEM inversion by adjoint source estimation

Pengliang Yang¹

¹ School of Mathematics, Harbin Institute of Technology, 150001, Harbin, China
E-mail: ypl.2100@gmail.com

December 1, 2022

Abstract

Marine controlled-source electromagnetic (CSEM) method has proved its potential in detecting highly resistive hydrocarbon bearing formations. A novel frequency domain CSEM inversion approach using fictitious wave domain time stepping modelling is presented. Using Lagrangian-based adjoint state method, the inversion gradient with respect to resistivity can be computed by the product between the forward and adjoint fields. Simulation of the adjoint field using the same modelling engine is challenging as it requires time domain adjoint source time functions while only a few discrete frequencies of the data residual are available for the inversion. A regularized linear inverse problem is formulated in order to estimate a long time series from very few frequency samples. It can then be solved using linear optimization technique, yielding a matrix-free implementation. Instead of computing adjoint source time function one by one at each receiver location, a basis function implementation has been developed such that the inverse problem can be solved only once and reused every time to construct all time-domain adjoint sources. The method allows computing all frequencies of the EM fields in one go without heavy memory and computational overhead, making efficient 3D CSEM inversion feasible. Numerical examples are employed to demonstrate the application of our method.

1 Introduction

Controlled-source electromagnetic (CSEM) method is a well established technology to do geophysical exploration (Chave and Cox, 1982; Constable et al., 1986). It can also be configured for air-borne (Chang-Chun et al., 2015) and cross-well (Alumbaugh and Newman, 1997) geometries. Land CSEM has been a commonplace to find mineral deposit (Ward and Hohmann, 1988; Zhdanov and Keller, 1994; Grayver et al., 2014). As a complement to seismic measurement, marine CSEM have been successfully applied to detect hydrocarbon bearing formations in oil and gas industry (Eidesmo et al., 2002; Ellingsrud et al., 2002; Constable and Srnka, 2007; MacGregor and Tomlinson, 2014), using an active electric dipole source towed by a vessel over an array of seafloor receivers. The key to these applications is the good sensitivity of the electromagnetic signals to distinguish high contrast in resistivity between saline-filled rocks and hydrocarbons (Abubakar et al., 2008). This property makes CSEM an ideal tool for de-risking (MacGregor et al., 2007) in reservoir exploration prior to drilling, as well as 4D monitoring applications during production (Shantsev et al., 2020). A nice topical review on marine CSEM inversion has been given in Constable (2010).

CSEM inversion has been a standard technique to translate CSEM data into electrical properties of the subsurface. To determine the resistivity model, a nonlinear inverse problem is then formulated to iteratively minimize the difference between the observed EM data and the synthetic data derived from numerical modelling, using different optimization schemes, such as nonlinear conjugate gradient method (Gribenko and Zhdanov, 2007; Commer and Newman, 2008), quasi-Newton l-BFGS (Plessix and Mulder, 2008; Schwarzbach and Haber, 2013), and Gauss-Newton method (Constable et al., 1987; Abubakar et al., 2008; Zaslavsky et al., 2013).

The kernel of CSEM inversion is the numerical simulation of 3D electromagnetic field propagation, which is computationally expensive. There are many studies on diffusive electromagnetic modelling using different methods, for example, the time-domain finite-difference method (Oristaglio and Hohmann, 1984; Wang and Hohmann, 1993; Taflove and Hagness, 2005), the frequency-domain finite-difference method (Newman and Alumbaugh, 1995; Smith, 1996a; Mulder, 2006; Streich, 2009), and the frequency-domain finite-element method (Li and Key, 2007; da Silva et al., 2012; Key, 2016; Rochlitz et al., 2019).

Due to the diffusive nature of low-frequency CSEM fields, most of the 3D CSEM modelling schemes resort to the frequency domain solution of the Maxwell equation to avoid the high computational cost dictated by

the restrictive stability condition for direct solution in the time domain. Both the frequency domain finite difference method and finite element method formulate Maxwell equation as a matrix-based linear system, which may be solved using direct (Streich, 2009) or iterative (Smith, 1996b; Mulder, 2006; Puzyrev et al., 2013) solvers. Modelling by direct solver is very attractive for multi-source CSEM problems (Streich, 2009), as the matrix system can be factorized only once and reused for all sources by forward-backward substitution. Since the inversion of the large sparse matrix for 3D problems involves huge amount of memory resources, direct methods may easily go beyond the memory capacity of a desktop computer. Iterative solvers require much less memory storage but may be time-consuming and difficult to converge due to ill-conditioning of the discretized Helmholtz matrix when the conductivity/resistivity model is highly heterogeneous or the modelling grid is severely stretched (Mulder, 2006). While the frequency domain finite element method is flexible to address complex model geometries thanks to the pre-computed meshes, the meshing in 3D geometries using tetrahedral and hexahedral mesh itself is a challenging and time consuming task.

In the time-domain, the fields are updated at each time step, allowing the modelling over the same memory units. The frequency domain fields can be integrated on the fly during time-stepping, such that multiple frequencies can be extracted from the same simulation. This avoids repeating several times of the modelling for different frequencies in frequency domain methods. It motivates Maaø (2007) to propose a modified wave domain approach to significantly speed up the computation of diffusive electromagnetic modelling. The method has been adapted in Støren et al. (2008) to efficiently compute the inversion gradient for 3D industrial scale applications. The modified wave domain approach by Maaø (2007) has an attenuation/diffusive term. Inspired by the fictitious wave domain approach initially proposed in Lee et al. (1989), Mittet (2010) transformed the diffusion domain Maxwell equation into a pure wave domain.

A straightforward time-domain discretization of the diffusive Maxwell equation leads to the temporal sampling proportional to the square of grid spacing, due to the requirement of the stability condition ($\Delta t \propto \Delta x^2$). This means taking half the spatial sampling will lead to a quadratic increase of the number of time steps for a simulation of the same duration. Transforming the diffusive domain into wave domain using fictitious wave domain approach allows a linear increase of time step with the use of finer grid spacing ($\Delta t \propto \Delta x$). This yields a highly efficient computing scheme to compute the same frequency domain EM field, as it significantly reduces the required number of time steps. These advantages inspire us to adopt the fictitious wave domain method for CSEM inversion.

The major contribution of this paper is to develop an efficient frequency domain CSEM inversion scheme based on the fictitious wave domain modelling. By formulating the frequency-domain CSEM inversion using Lagrangian-based adjoint state method, the gradient of the misfit functional requires both a forward and an adjoint field. Efficient computation of the frequency domain adjoint field by time domain modelling manifests itself as a major challenge in this development as it requires the time domain adjoint source time functions at all receiver locations which are unavailable due to the formulation of CSEM inversion in frequency domain. The key novelty of our approach is to estimate the time-domain adjoint source time function based on only a few discrete frequency samples of the data residual. To do so, we formulate a regularized linear inverse problem, and then present an efficient, matrix-free implementation using very few basis functions. The linear inverse problem can be solved only once and the resulting solution can be reused to derive the adjoint source time functions at all receiver locations. This novel development delivers an efficient 3D CSEM inversion methodology in fictitious wave domain. We finally apply our method to two examples for numerical demonstration.

2 CSEM modelling in fictitious wave domain

The Maxwell equations in a quasi-static regime (i.e., with negligible effect of displacement currents) are written in the time domain

$$\begin{cases} \nabla \times \mathbf{E} + \mu \partial_t \mathbf{H} = \mathbf{M} \\ \nabla \times \mathbf{H} - \sigma \mathbf{E} = \mathbf{J} \end{cases} \quad (1)$$

or in the frequency domain

$$\begin{cases} \nabla \times \mathbf{E} - i\omega \mu \mathbf{H} = \mathbf{M} \\ \nabla \times \mathbf{H} - \sigma \mathbf{E} = \mathbf{J} \end{cases}, \quad (2)$$

where the electrical and magnetic fields are vectors consisting of 3 components, viz., $\mathbf{E} = (E_x, E_y, E_z)^T$, $\mathbf{H} = (H_x, H_y, H_z)^T$; $\mathbf{J} = (J_x, J_y, J_z)^T$ and $\mathbf{M} = (M_x, M_y, M_z)^T$ stand for electrical and magnetic sources, respectively. We slightly abuse the same notation to denote the same quantity when switching between time domain and frequency domain, where the convention of Fourier transform $\partial_t \leftrightarrow -i\omega$ has been adopted. The magnetic permeability is μ . The conductivity is a symmetric 3×3 tensor, i.e., $\sigma_{ij} = \sigma_{ji}$, $i, j \in \{x, y, z\}$. The

isotropic medium means only the diagonal elements of the conductivity tensor are non-zeros and the same in all directions: $\sigma_{xx} = \sigma_{yy} = \sigma_{zz}$; $\sigma_{ij} = 0, i \neq j$. The vertical transverse isotropic (VTI) medium still has only the diagonal elements, that is, $\sigma_h := \sigma_{xx} = \sigma_{yy}$, $\sigma_v = \sigma_{zz}$, where σ_h and σ_v stand for horizontal conductivity and vertical conductivity, respectively. The resistivity is defined as the inverse of the conductivity, i.e., $\rho_{ij} = 1/\sigma_{ij}$.

To achieve efficient modelling in the time-domain, we transform the above system from diffusion to wave domain, following Mittet (2010). The idea is to define a fictitious di-electrical permittivity in equation (2) as $\sigma = 2\omega_0\varepsilon$, while multiplying the 2nd equation in equation (2) with $\sqrt{-i\omega/2\omega_0}$, leading to

$$\begin{cases} \nabla \times \underbrace{\mathbf{E}}_{\mathbf{E}'} + \underbrace{\mu \sqrt{-i2\omega\omega_0}}_{-i\omega'} \underbrace{\sqrt{\frac{-i\omega}{2\omega_0}} \mathbf{H}}_{\mathbf{H}'} = \mathbf{M} \\ \nabla \times \underbrace{\sqrt{\frac{-i\omega}{2\omega_0}} \mathbf{H}}_{\mathbf{H}'} - \underbrace{\sqrt{-i2\omega\omega_0}}_{-i\omega'} \varepsilon \mathbf{E} = \underbrace{\sqrt{\frac{-i\omega}{2\omega_0}} \mathbf{J}}_{\mathbf{J}'} \end{cases} \quad (3)$$

where a prime is introduced to define the resulting fields in the wave domain. Equation (3) can then be transformed into time domain as

$$\begin{cases} \nabla \times \mathbf{E}' + \mu \partial_t \mathbf{H}' = \mathbf{M}' \\ \nabla \times \mathbf{H}' - \varepsilon \partial_t \mathbf{E}' = \mathbf{J}' \end{cases}, \quad (4)$$

which allows us to do efficient modelling using leap-frog finite-difference time-domain (FDTD) method over the staggered grid. From the electromagnetic fields in the time domain, the frequency domain fields can be integrated on the fly during time stepping modelling thanks to the discrete time Fourier transform (DTFT):

$$u(\mathbf{x}, \omega'_m; \mathbf{x}_s) = \sum_{n=0}^{N_t-1} u(\mathbf{x}, t_n; \mathbf{x}_s) \exp(i\omega'_m t_n), \quad m = 1, \dots, N_\omega \quad (5)$$

where $u(\mathbf{x}, t; \mathbf{x}_s) \in \{E'_x, E'_y, E'_z, H'_x, H'_y, H'_z\}$ denotes the electric/magnetic field at the spatial location $\mathbf{x} \in X$ and the time $t_n = n\Delta t$ excited by a source from the spatial location x_s ; N_t is the total number of time steps that the frequency domain field $u(x, \omega'; x_s)$ reaches its steady state, while N_ω is the number of discrete frequencies, usually $N_\omega \ll N_t$. It is possible to check the convergence of the field regularly during the modelling to avoid additional time steppings which have negligible contributions to the time integral.

It should be noted that in the fictitious wave domain approach the complex-valued frequency $\omega' = (1+i)\sqrt{\omega\omega_0}$ is the key to realize the attenuation effect of diffusive EM field during time evolution. Disguising a diffusive phenomenon as a wave event will not change the diffusive nature of the underlying physics. The fictitious wave domain modelling is simply a mathematical tool to efficiently compute frequency domain EM fields: multiple frequencies can be integrated on the fly during the same time stepping procedure. These advantages make the method attractive for forward modelling.

3 Fictitious wave domain CSEM inversion

The CSEM inversion is an iterative nonlinear optimization procedure. At each iteration, the gradient of the data misfit with respect to conductivity can be computed via the product between forward and adjoint fields. To use fictitious wave domain modelling engine for adjoint simulation, we present a novel approach to estimating the adjoint source time functions by formulating a regularized linear inverse problem. An in-depth analysis shows that this linear inverse problem needs to be solved only once to result in a limited number of basis functions, which can then be used to construct the time-domain adjoint source at different receiver locations. This key development enables efficient and practical 3D CSEM inversion by fictitious wave domain modelling engine.

3.1 CSEM inverse problem

The Maxwell equations forms a linear system as

$$\underbrace{\begin{bmatrix} -\sigma & \nabla \times \\ \nabla \times & -i\omega\mu \end{bmatrix}}_{\mathbf{A}(m)} \underbrace{\begin{bmatrix} \mathbf{E} \\ \mathbf{H} \end{bmatrix}}_{\mathbf{u}} = \underbrace{\begin{bmatrix} \mathbf{J} \\ \mathbf{M} \end{bmatrix}}_{\mathbf{f}}, \quad (6)$$

where the electromagnetic propagator $\mathbf{A}(m)$ is a linear operator applied to the vector field \mathbf{u} , which gathers electrical and magnetic fields (each component has been denoted by $u := u(\mathbf{x}, \omega; \mathbf{x}_s)$ in the previous section).

The source vector with nonzero excitation at the source location \mathbf{x}_s is prescribed by $\mathbf{f} := \mathbf{f}(\mathbf{x}, \omega; \mathbf{x}_s)$. Note that all field variables are functions of both frequency and space ($u(\mathbf{x}, \omega; \mathbf{x}_s)$, $\mathbf{x} \in X, \omega \in \Omega$), while the medium property is only a function of space ($m(\mathbf{x})$, $\mathbf{x} \in X$), which can be the conductivity σ_{ij} or the permeability μ .

To find the resistivity of the subsurface, the data misfit is defined in least-squares sense

$$\phi_d(m) = \frac{1}{2} \left\| \underbrace{\begin{bmatrix} \mathbf{W}_1 & 0 \\ 0 & \mathbf{W}_2 \end{bmatrix}}_{\mathbf{W}} \left(\underbrace{\begin{bmatrix} \mathbf{E}_{obs}(\mathbf{x}_r, \omega; \mathbf{x}_s) \\ \mathbf{H}_{obs}(\mathbf{x}_r, \omega; \mathbf{x}_s) \end{bmatrix}}_{\mathbf{d}(\mathbf{x}_r, \omega; \mathbf{x}_s)} - \underbrace{\begin{bmatrix} \mathbf{E}(\mathbf{x}_r, \omega; \mathbf{x}_s) \\ \mathbf{H}(\mathbf{x}_r, \omega; \mathbf{x}_s) \end{bmatrix}}_{\mathbf{d}_{syn}(\mathbf{x}_r, \omega; \mathbf{x}_s)[m]} \right) \right\|^2 \quad (7)$$

where $\mathbf{d}(\mathbf{x}_r, \omega; \mathbf{x}_s)$ denotes the observed data at the receiver location \mathbf{x}_r due to the source at the location \mathbf{x}_s , while the synthetic data $\mathbf{d}_{syn}(\mathbf{x}_r, \omega; \mathbf{x}_s)[m] := \mathbf{u}(\mathbf{x}_r, \omega; \mathbf{x}_s) = \mathbf{R}\mathbf{u}(\mathbf{x}, \omega; \mathbf{x}_s)$ (simulated with the model parameter m) are extracted by the restriction operator \mathbf{R} from the modelled wavefield at the receiver location $u(\mathbf{x}_r, \omega; \mathbf{x}_s) = \int_X u(\mathbf{x}, \omega; \mathbf{x}_s) \delta(\mathbf{x} - \mathbf{x}_r) d\mathbf{x}$, $\mathbf{x} \in X, \omega \in \Omega$, where $u(\mathbf{x}_r, \omega; \mathbf{x}_s)$ is one component of the vector field $\mathbf{u}(\mathbf{x}_r, \omega; \mathbf{x}_s)$. In the remainder of the paper, we shall drop the dependence of $(\mathbf{x}_r, \omega; \mathbf{x}_s)$ and the summation over sources and receivers without loss of clarity unless clearly stated if necessary. Two weighting matrices, \mathbf{W}_1 and \mathbf{W}_2 together forming the diagonal weighting matrix \mathbf{W} , are employed to weight the electric and magnetic fields respectively. These weighting matrices may be specified according to the uncertainty model in terms of the real acquisition and the equipment (Mittet and Morten, 2012). If the magnetic data are not considered in the inversion, we simply set $\mathbf{W}_2 = 0$.

In the CSEM settings, the magnetic permeability μ is considered as the same constant as in the vacuum. We are interested in retrieving the conductivity σ (or the resistivity $\rho = 1/\sigma$) which may exhibit anisotropy. Denote the adjoint field $\mathbf{v} = (\mathbf{E}, \mathbf{H})^T$. According to (28), a generic expression of the gradient of the data misfit with respect to the medium parameter m is

$$\frac{\partial \phi_d(m)}{\partial m} = \Re \sum_{\omega} \bar{\mathbf{v}}^T \frac{\partial \mathbf{A}(m)}{\partial m} \mathbf{u}, \quad (8)$$

yielding

$$\frac{\partial \phi_d}{\partial \sigma_{ij}} = -\Re \sum_{\omega} \bar{E}_j \cdot E_i, \quad i, j \in \{x, y, z\}. \quad (9)$$

For commonly used VTI medium, the gradients of the misfit with respect to horizontal conductivity σ_h and vertical conductivity σ_v are

$$\frac{\partial \phi_d}{\partial \sigma_h} = -\Re \sum_{\omega} (\bar{E}_x \cdot E_x + \bar{E}_y \cdot E_y), \quad \frac{\partial \phi_d}{\partial \sigma_v} = -\Re \sum_{\omega} \bar{E}_z \cdot E_z. \quad (10)$$

In isotropic medium ($\sigma_{ii} = \sigma$, $i = x, y, z$), we have the simple gradient expression

$$\frac{\partial \phi_d}{\partial \sigma} = -\Re \sum_{\omega} \mathbf{E}^\dagger \cdot \mathbf{E} = -\Re \sum_{\omega} (\bar{E}_x \cdot E_x + \bar{E}_y \cdot E_y + \bar{E}_z \cdot E_z). \quad (11)$$

The derivation of the above expressions is trivial using adjoint state method, see Appendix.

3.2 Adjoint modelling in fictitious wave domain

To facilitate the computation of the adjoint field and the inversion gradient, one may take the conjugate of equation (27):

$$\mathbf{A}^T(m) \bar{\mathbf{v}} = \overline{\mathbf{R}^T \mathbf{W}^T \mathbf{W} (\mathbf{d} - \mathbf{R}\mathbf{u})}. \quad (12)$$

Since $\mathbf{A}^T(m) = \mathbf{A}(m)$, the above operation allows us to use the same modelling engine to compute the conjugate of the adjoint field, as long as proper adjoint source can be provided for adjoint simulation. Equation (12) shows that the adjoint field can be computed using only one modelling, provided that a time-domain adjoint source time function is available and then injected at once to do time-domain simulation. This is ensured by the superposition principle thanks to the linearity of the Maxwell equation.

Unfortunately, for CSEM inversion in the frequency domain, only few discrete frequencies are available, leading to the adjoint source (i.e. the data residual) specified only at few discrete frequencies. A time domain adjoint source is therefore not directly accessible. Switching from diffusive frequency domain back to fictitious time domain with wave should be understood as a linear transformation rather than the true inverse Fourier transform. This is because the mapping of fictitious transform is not bijective, as the number of time steps

N_t for numerical simulation is significantly larger than the number of discrete frequencies N_ω used for CSEM investigation ($N_\omega \ll N_t$). There exists an infinite number of time series which may match the few discrete frequencies. Searching for the inverse is therefore an under-determined problem.

Let us denote the right hand side of equation (12) at a specific receiver location as $s(\omega')$. To retrieve a long time series for adjoint modelling, a linear inverse problem is formulated to convert the adjoint source $s(\omega')$ from frequency to time domain based on DFT in equation (5) by minimizing the following misfit functional

$$\begin{aligned} \Psi &= \sum_{m=1}^{N_\omega} |s(\omega'_m) - \sum_{n=0}^{N_t-1} e^{i\omega'_m t_n} s(t_n)|^2 + \gamma \sum_{n=0}^{N_t-1} |s(t_n)|^2 \\ &= \sum_{m=1}^{N_\omega} \left(|\Re\{s(\omega'_m)\} - \sum_{n=0}^{N_t-1} e^{-\sqrt{\omega_m \omega_0} t_n} \cos(\sqrt{\omega_m \omega_0} t_n) s(t_n)|^2 \right. \\ &\quad \left. + |\Im\{s(\omega'_m)\} - \sum_{n=0}^{N_t-1} e^{-\sqrt{\omega_m \omega_0} t_n} \sin(\sqrt{\omega_m \omega_0} t_n) s(t_n)|^2 \right) + \gamma \sum_{n=0}^{N_t-1} |s(t_n)|^2 \end{aligned}$$

where \Im takes the imaginary part of the complex variable. If we discretize the time as $t_n = n\Delta t$ and define

$$\mathbf{s}(\omega') := \begin{bmatrix} \Re\{s(\omega'_1)\} \\ \vdots \\ \Re\{s(\omega'_{N_\omega})\} \\ \Im\{s(\omega'_1)\} \\ \vdots \\ \Im\{s(\omega'_{N_\omega})\} \end{bmatrix}, \mathbf{s}(t) := \begin{bmatrix} s(t_0) \\ \vdots \\ s(t_{N_t-1}) \end{bmatrix} \quad (13)$$

and

$$\mathbf{B} := \begin{bmatrix} e^{-\sqrt{\omega_1 \omega_0} t_0} \cos(\sqrt{\omega_1 \omega_0} t_0) & \cdots & e^{-\sqrt{\omega_1 \omega_0} t_{N_t-1}} \cos(\sqrt{\omega_1 \omega_0} t_{N_t-1}) \\ \vdots & \ddots & \vdots \\ e^{-\sqrt{\omega_{N_\omega} \omega_0} t_0} \cos(\sqrt{\omega_{N_\omega} \omega_0} t_0) & \cdots & e^{-\sqrt{\omega_{N_\omega} \omega_0} t_{N_t-1}} \cos(\sqrt{\omega_{N_\omega} \omega_0} t_{N_t-1}) \\ e^{-\sqrt{\omega_1 \omega_0} t_0} \sin(\sqrt{\omega_1 \omega_0} t_0) & \cdots & e^{-\sqrt{\omega_1 \omega_0} t_{N_t-1}} \sin(\sqrt{\omega_1 \omega_0} t_{N_t-1}) \\ \vdots & \ddots & \vdots \\ e^{-\sqrt{\omega_{N_\omega} \omega_0} t_0} \sin(\sqrt{\omega_{N_\omega} \omega_0} t_0) & \cdots & e^{-\sqrt{\omega_{N_\omega} \omega_0} t_{N_t-1}} \sin(\sqrt{\omega_{N_\omega} \omega_0} t_{N_t-1}) \end{bmatrix} \quad (14)$$

the objective of the above linear inverse problem can be compactly written in matrix form

$$\Psi = \|\mathbf{s}(\omega') - \mathbf{B}\mathbf{s}(t)\|^2 + \gamma \|\mathbf{s}(t)\|^2, \quad (15)$$

where a regularization term taking into account the minimum energy of the solution has been penalized by a parameter γ to stabilize the linear inversion and to determine a unique solution. Note that the complex factors have been splitted into real and imaginary part. To solve this ill-posed problem, regularization has been introduced to the inversion of the matrix $\mathbf{B} \in \mathbb{R}^{2N_\omega \times N_t}$. The solution $\mathbf{s}(t)$ can easily be found using linear optimization algorithms, e.g. LSQR (Paige and Saunders, 1982) and the conjugate gradient method for the resulting normal equation (CGNR) (Saad, 2003). Based on the frequency and time index, the each element of \mathbf{B} can be formed on the fly when computing matrix vector product, implying a matrix free implementation.

It is emphasized that our method relies on fictitious wave domain formulation. Indeed, Mittet (2010) proposed another method to calculate the adjoint source time function by superposition of delayed causal wavelets. However, it leads to a nonlinear inverse problem which is very difficult to solve. Clearly, embedding a linear inverse problem in a nonlinear inverse problem is a much better option than embedding double nonlinear inverse problems. The truncated singular value decomposition (SVD) have been applied (Støren et al., 2008) to invert for an adjoint source, following the modified wave domain formulation of Maaø (2007). Mathematically, our approach using damped least-squares should give the same solution as the one from truncated SVD, since SVD is equivalent to finding the Moore-Penrose pseudo-inverse for \mathbf{B} (Björck, 1996, theorem 1.2.10 in p. 15, and section 2.7.2, p. 101). However, our empirical experience shows that the approximate inverse given by SVD suffers from numerical instability while consuming too much memory. The above linear inversion method gets rid of these issues, incorporating all frequencies in one run with better memory and computational efficiency.

3.3 A matrix-free basis function implementation

Let us denote $\mathbf{B}^+ = (\mathbf{B}^T \mathbf{B} + \gamma \mathbf{I})^{-1} \mathbf{B}^T \in \mathbb{R}^{N_t \times 2N_\omega}$ the Moore-Penrose pseudo-inverse of $\mathbf{B} \in \mathbb{R}^{2N_\omega \times N_t}$ such that

$$\mathbf{s}(t) = \mathbf{B}^+ \mathbf{s}(\omega). \quad (16)$$

The matrix \mathbf{B}^+ may be written down using the $2N_\omega$ columns:

$$\mathbf{B}^+ = [\mathbf{b}_1, \dots, \mathbf{b}_{N_\omega}, \mathbf{b}_{N_\omega+1}, \dots, \mathbf{b}_{2N_\omega}] \quad (17)$$

in which $\mathbf{b}_i \in \mathbb{R}^{N_t}$ is the i -th column of \mathbf{B}^+ . As a result, equation (16) translates into

$$\mathbf{s}(t) = \sum_{i=1}^{N_\omega} \Re\{s(\omega_i)\}\mathbf{b}_i + \Im\{s(\omega_i)\}\mathbf{b}_{i+N_\omega}. \quad (18)$$

It then becomes clear that the columns of \mathbf{B}^+ are the very few number of basis functions to construct the adjoint source time function. Given Δt and N_t , these basis functions are uniquely determined, hence independent of the frequency spectrum $s(\omega)$ (which are simply the coefficients for the linear combination of these basis functions). This means the iterative solution procedure needs to be performed only once to find all \mathbf{b}_i , which can then be used for each receiver locations to infer the corresponding adjoint source time function. Equation (18) also gives a recipe to efficiently compute these functions:

- If we set $\Re\{s(\omega_i)\} = 1$, $\Im\{s(\omega_i)\} = 0$ and $\Re\{s(\omega_j)\} = \Im\{s(\omega_j)\} = 0$ ($j \neq i$), we obtain $\mathbf{s}(t) = \mathbf{b}_i$.
- If we set $\Im\{s(\omega_i)\} = 1$, $\Re\{s(\omega_i)\} = 0$ and $\Re\{s(\omega_j)\} = \Im\{s(\omega_j)\} = 0$ ($j \neq i$), we obtain $\mathbf{s}(t) = \mathbf{b}_{i+N_\omega}$.

By repeatedly feeding the iterative optimization algorithm $2N_\omega$ times using different Dirac delta input $\mathbf{s}(\omega) = (0, \dots, 0, 1, 0, \dots, 0)^T$, we obtain the $2N_\omega$ columns of \mathbf{B}^+ .

Figure 1 gives an example of these basis functions using the parameters $\Delta t = 0.002$, $N_t = 1000$ and $f_0 = 1$ and $N_\omega = 3$. To solve this linear optimization problem, Claerbout's conjugate gradient algorithm (Claerbout and Fomel, 2008) (which is essentially a CGNR algorithm according to Saad (2003)) has been applied. As can be seen from Figure 2, within 15 CG iterations, the proposed method leads to highly accurate estimation for these basis functions, with the error less than 10^{-8} . In this test, the regularization parameter γ was chosen to be 10^{-3} . It is found the shape of the basis functions do not change much using different choices of γ , indicating that the method is robust.

For different receiver locations, the data residuals in the frequency domain may be dramatically different, but these basis functions are the same. We therefore only solve the above regularized linear inverse problem once to construct all adjoint source time functions through their linear combination. The frequency domain data residuals gives the weighting coefficients to modulate these basis.

3.4 The final algorithm

The total misfit functional for CSEM inversion consists of both data fitting and model regularization:

$$\phi(m) = \phi_d(m) + \beta\phi_m(m), \quad (19)$$

where $\phi_m(m)$, penalized by the parameter β , is the model misfit term to enforce smoothness on the inverted model. A popular choice is to use Tikhonov regularization to minimize the roughness of the model compared with a reference model m_{ref} , i.e., $\phi_m(m) = \frac{1}{2}\|\nabla^\alpha(m - m_{ref})\|^2$, where the anisotropic first order difference operator $\nabla^\alpha = (\alpha_x\partial_x, \alpha_y\partial_y, \alpha_z\partial_z)^T$ with coefficients α_x , α_y and α_z can be tuned by the user. This leads to the total gradient of the misfit functional prescribed by $\frac{\partial\phi}{\partial m} = \frac{\partial\phi_d}{\partial m} + \frac{\partial\phi_m}{\partial m}$. Based on the gradient information computed above, a descent direction δm^k can then be constructed to iteratively update the model parameters $m^{k+1} = m^k + \alpha\delta m^k$, where α is the step length estimated by line search method. In this paper, the descent direction δm^k at the k -th iteration is computed using l-BFGS algorithm (Nocedal and Wright, 2006) by storing the gradients in the previous iterations.

It is worth noting that the inversion gradient computed using the proposed approach is approximate rather than exact. Consequently, the descent direction estimated using l-BFGS after several iterations may have difficulty to succeed in the line search procedure. I therefore propose to restart l-BFGS using the steepest descent direction after the first failure of the line search. The algorithm will eventually be terminated if the maximum number of iterations is reached.

The use of conductivity as model parameter creates some kinds of ill-conditioning due to its value varying in a large range (the seawater is around $0.3 \Omega \text{ m}$ while a thin layer of hydrocarbon bearing sediment is more than $100 \Omega \text{ m}$). To capture the high contrast of the parameter variations, the inversion is re-parameterized using the logarithmic transformation $m := \ln \rho$, which is a dimensionless parameter varying in a much smaller dynamic range. It should be remarked that there exists other types of parameter scaling, see another example in Abubakar et al. (2008). This re-parametrization gives a relation $\rho = e^m$. Switching the parametrization is trivial thanks to the chain rule: $\frac{\partial\phi}{\partial m} = \frac{\partial\rho}{\partial m} \cdot \frac{\partial\sigma}{\partial\rho} \cdot \frac{\partial\phi}{\partial\sigma} = -\frac{1}{\rho} \frac{\partial\phi}{\partial\sigma}$. During the iterative inversion, the model parameter may be bounded within an upper bound m_{\max} and a lower bound m_{\min} according to a priori knowledge. These bounds help to stabilize the inversion in a more physically sensible manner.

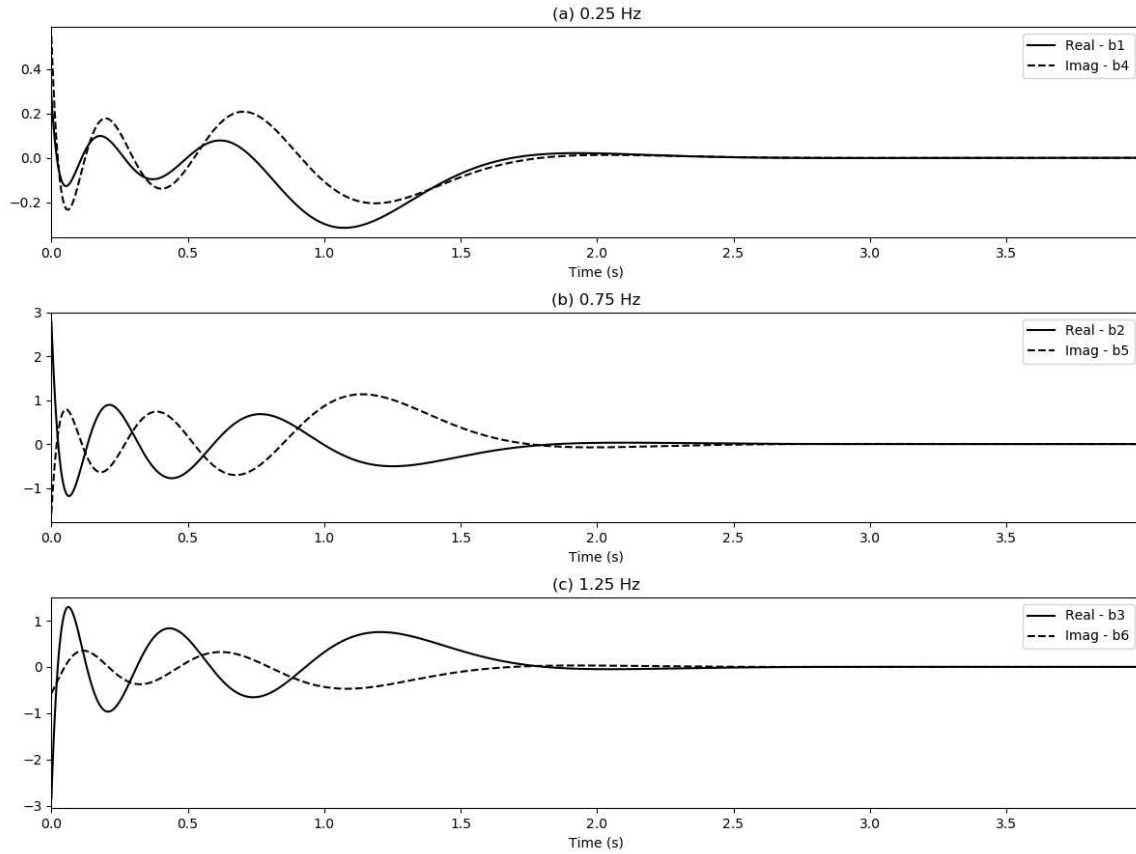


Figure 1: The basis functions using the parameters $\Delta t = 0.004$, $N_t = 1000$ and $N_\omega = 3$. The amplitude of these basis functions decays to zero with the increase of the time, which is quite suitable for frequency domain EM fields converging to steady state after simulation using sufficient number of time steps.

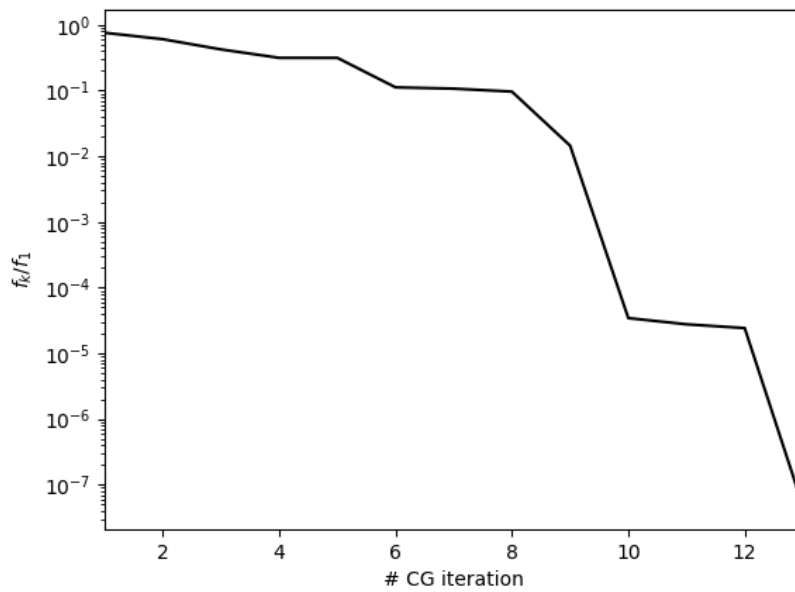


Figure 2: The convergence of CG iterations for the solution of basis functions

4 Numerical results

In this section we present two numerical examples to demonstrate the application of our method. The two examples are designed to validate the gradient expressions for the isotropic (the first example) and the VTI anisotropic (the second example) cases. In both examples, I use in-line and azimuth data with E_x and E_y components. This motivates us to utilize the uncertainty model proposed in Morten et al. (2009) to compute the diagonal weight matrix \mathbf{W} in order to capture the varying sensitivity of broadside EM data. The regularization parameters are configured with $\beta = 0.01$ using a cooling factor 0.7 through iterations. We set $\alpha_x = \alpha_y = 1$ and $\alpha_z = 0.1$ in both tests. We choose the initial model as the reference model for both inverse exercises. To mitigate the weak sensitivity of the EM field to the deeper part of the model, a depth preconditioning has been applied following the work of Plessix and Mulder (2008). Taking into account that the number of source locations is much larger than the number of receivers, reciprocity can be applied to switch the sources and receivers to achieve better computational efficiency. The actual source used in the inversion is therefore the common receiver gather. The code is parallelized over the sources to achieve the best scaling performance since the sources are independent of each other.

4.1 A two-block model

Our first example is a two-block land model similar to the one presented in Grayver et al. (2013). The model has a background resistivity of $5 \Omega \text{ m}$, including two anomalies: a low resistivity inclusion of $1 \Omega \text{ m}$ and a high resistivity inclusion of $100 \Omega \text{ m}$, as shown in Figure 3a. The physical dimension of the model spans over a 3D domain $X = X_1 \times X_2 \times X_3$, where $X_1 = [-2000, 2000] \text{ m}$, $X_2 = [-2000, 2000] \text{ m}$ and $X_3 = [0, 1500] \text{ m}$. There are 16 receivers and 256 transmitters with equal distance on the surface of this model. Figure 4 gives the survey layout sheet of the acquisition geometry. The model has been discretized with the regular grid using $\Delta x = \Delta y = 60 \text{ m}$ and $\Delta z = 25 \text{ m}$. The observed data are generated at two frequencies: 0.25 Hz and 1 Hz. Figure 5 shows that the inversion runs for 30 iterations, arriving at a relatively low normalized misfit. The final inverted model is capable to retrieve both the low resistivity inclusion (Figure 6a) and the high resistivity inclusion (Figure 6b).

4.2 A marine CSEM example

In practical CSEM survey for reservoir exploration, a number of towlines using very low-frequency (0.1-10 Hz), high-energy electrical source will be deployed with hundreds of receivers. The source-receiver offset extends up to 10 km is very standard. Due to the limit of computer resource at hand, a 3D CSEM inversion is carried out for 20 iterations based on a model of size $X = X_1 \times X_2 \times X_3$, where $X_1 = X_2 = [-9000, 9000] \text{ m}$ and $X_3 = [0, 3000] \text{ m}$. Figure 7 displays the survey layout sheet for the test: 10 towlines (5 in x direction and 5 in y direction) are deployed in order to cover the region of interest. Each towline has 81 source locations with a separation of 200 m. The receivers (25 in total) are deployed at the crossings of these towlines.

As shown in Figure 8a, this synthetic model has relatively simple structure: the seawater is of $0.3 \Omega \text{ m}$ and the background sediment is of $1 \Omega \text{ m}$. The most striking feature is a disk-shaped resistor of $100 \Omega \text{ m}$ sitting at the depth between 1700 m and 1800 m, which mimics the canonical reservoir. The starting model for the inversion in Figure 8b is the same as the true model except the absence of the strong resistor.

A seafloor bathymetry with varying depth has been embedded in the model. The model is densely gridded around bathymetry and above, with the grid spacing $\Delta z = 30 \text{ m}$. The grid has been stretched with a constant growing factor at a certain distance below the seabed. To model the CSEM response as precise as possible, our newly developed high-order finite-difference time-domain method over non-uniform grid (Yang and Mittet, 2022) has been applied for numerical simulation.

Three frequencies (0.25 Hz, 0.75 Hz and 1 Hz) have been used to perform this inversion. Figure 9 shows that this CSEM inversion was converging well. After 20 l-BFGS iterations, we are able to reconstruct the vertical resistivity ($\rho_v = 1/\sigma_h$) and the horizontal resistivity $\rho_h = 1/\sigma_v$ at the location very close to the ground truth. The inverted vertical resistivity in Figure 9a is much better than the inverted horizontal resistivity: the resolution of ρ_v is better than the retrieved ρ_v . This is reasonable because the EM fields are vertically polarized in the thin resistive layer. The value of the retrieved ρ_v is higher than the retrieved ρ_h , while both are smaller than $100 \Omega \text{ m}$ and thicker than 100 m. It can be seen that the recovered anomaly in ρ_v is of 100-150 m shallower than the true location. This is because the CSEM response is proportional to the product of resistivity difference times the thickness (see an explanation in Mittet and Morten (2012)): lower resistivity with larger thickness may be able to create similar amplitude response compared with higher resistivity with thin depth distribution.

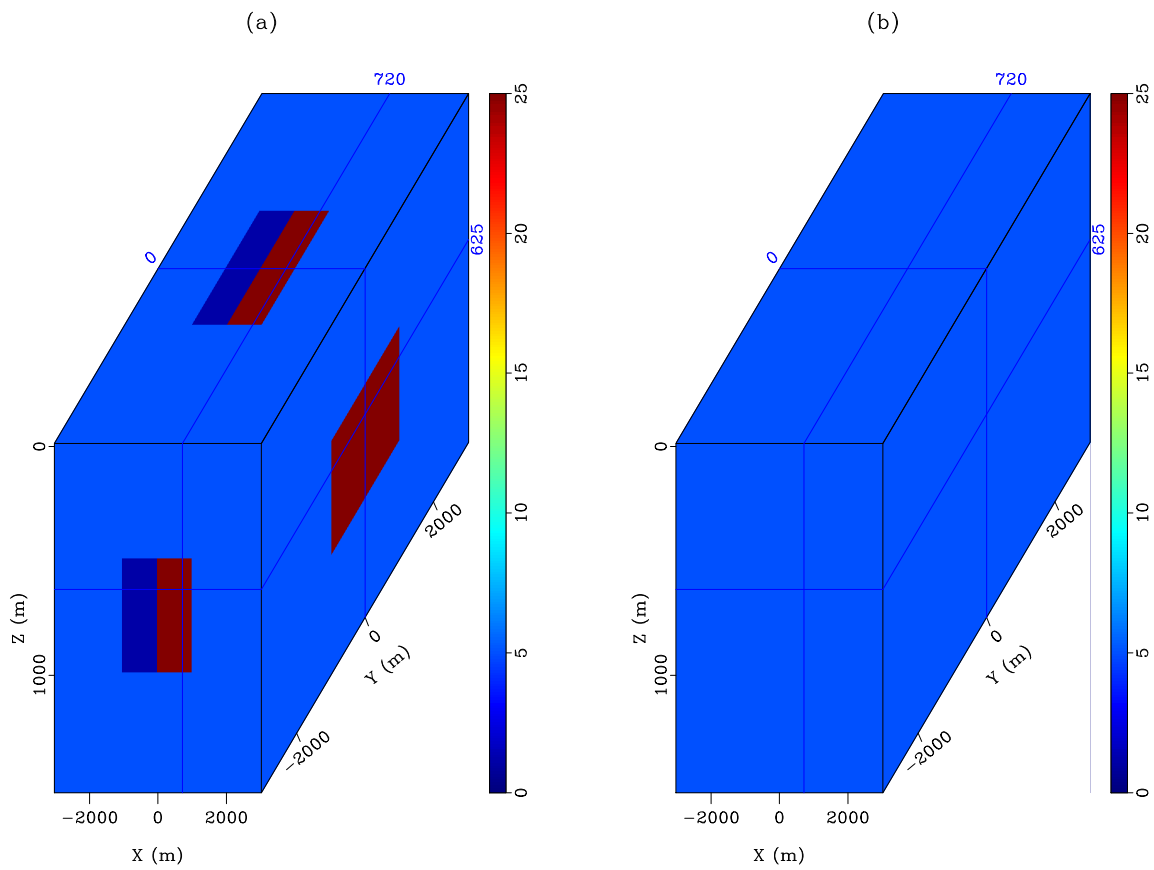


Figure 3: (a) The true land model ($5 \Omega \text{ m}$ background with two anomalous inclusions of $1 \Omega \text{ m}$ (left) and $100 \Omega \text{ m}$ (right)); (b) The homogeneous initial model of $5 \Omega \text{ m}$. The models are clipped at $25 \Omega \text{ m}$ for display purpose.

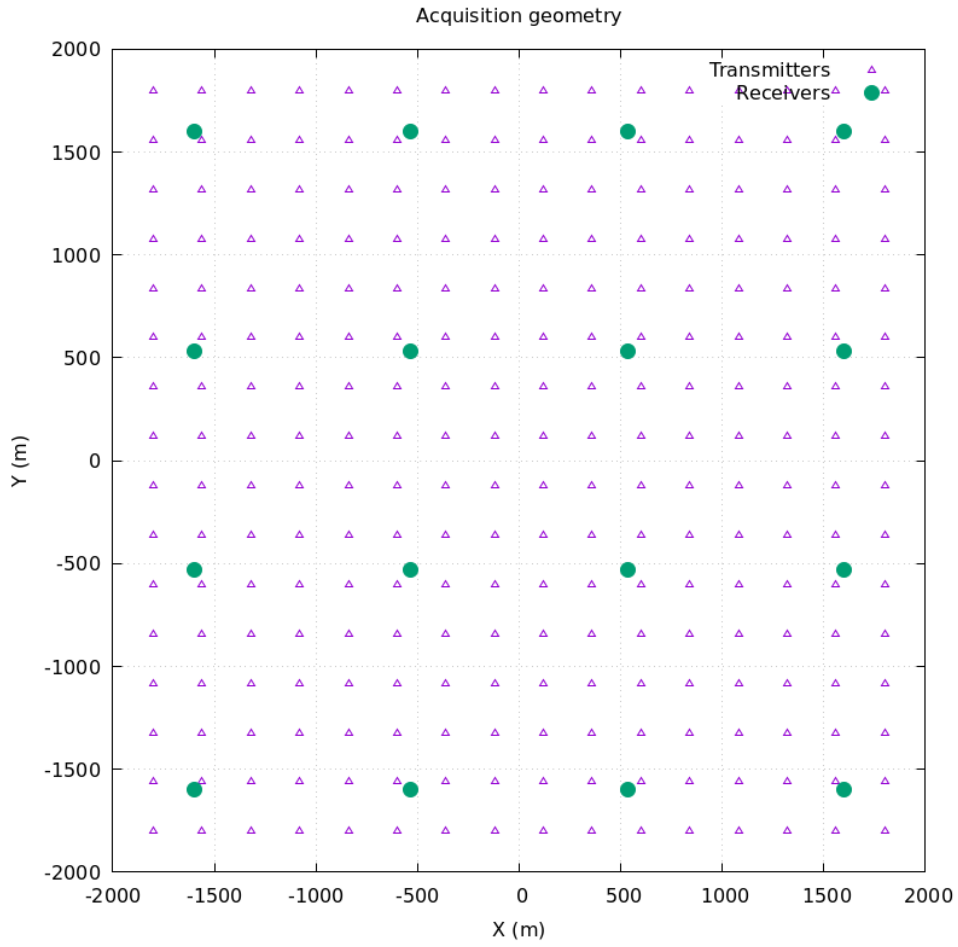


Figure 4: Survey layout sheet for the two-block model.

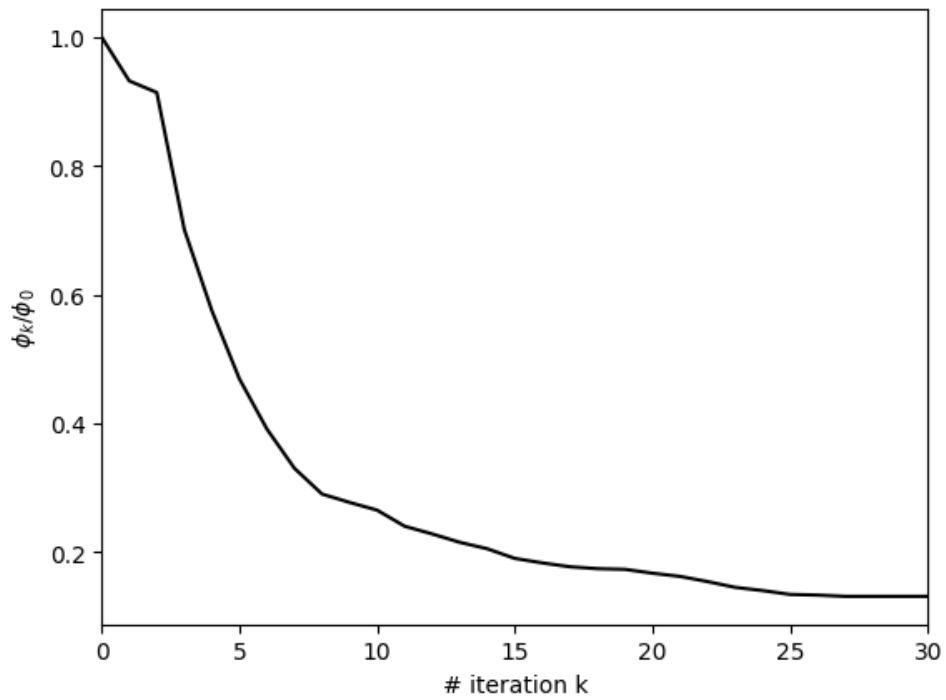


Figure 5: The convergence history in terms of the normalized misfit for the inversion of the two-block model.

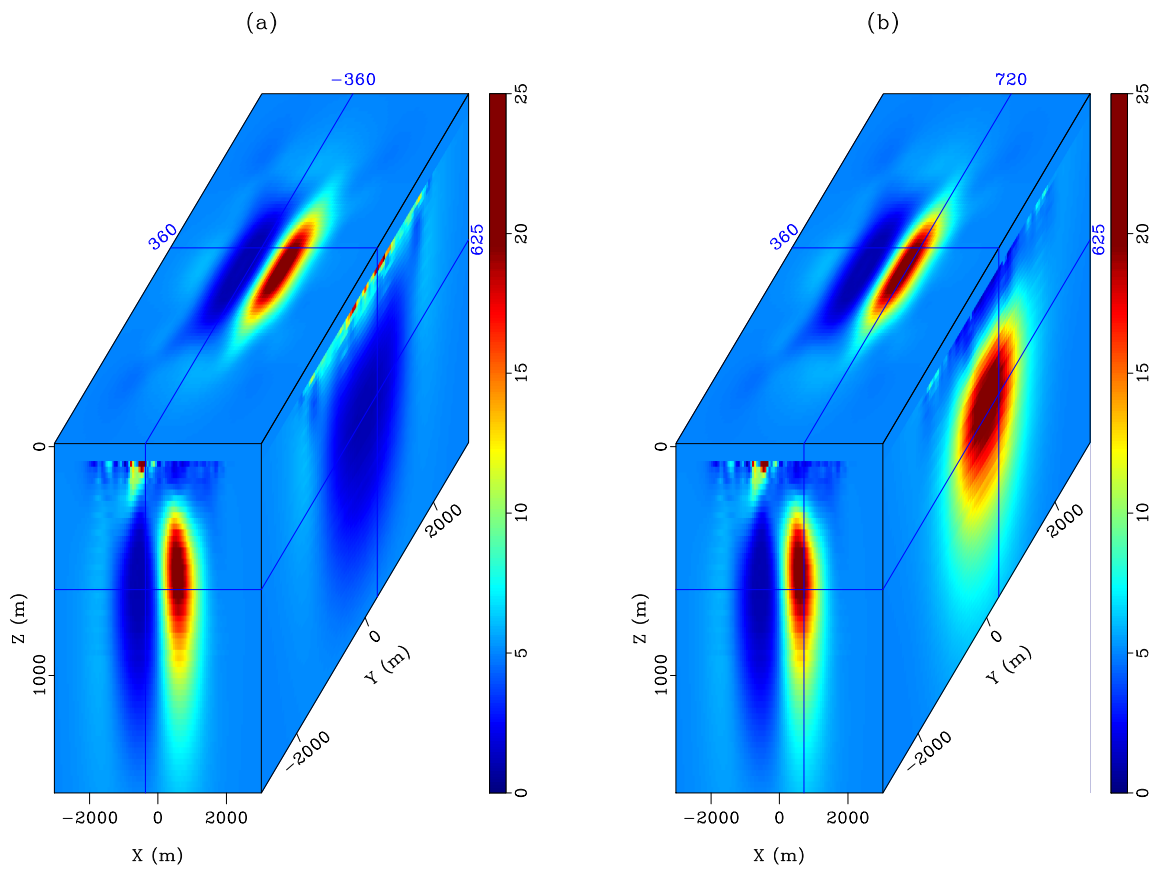


Figure 6: Inversion result for (a) low resistivity anomaly and (b) high resistivity anomaly.

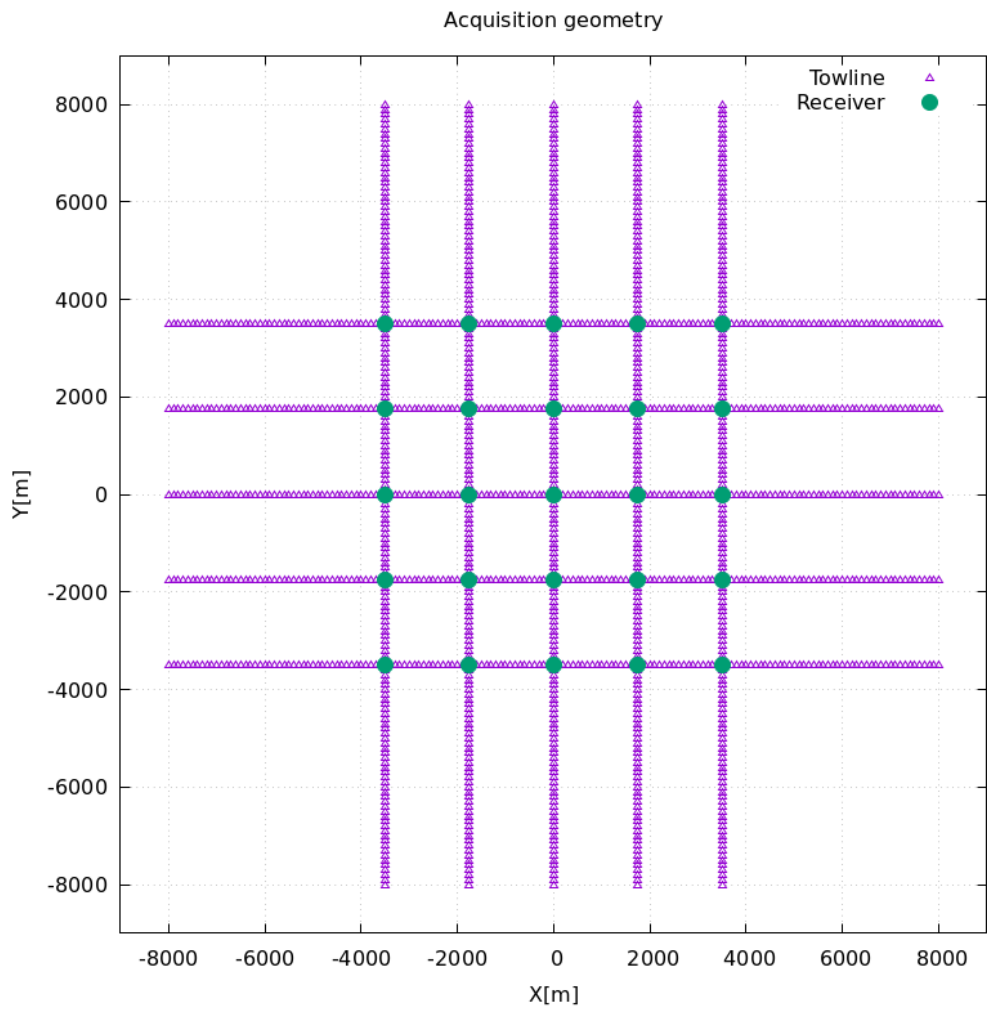


Figure 7: Survey layout sheet for marine CSEM inversion.

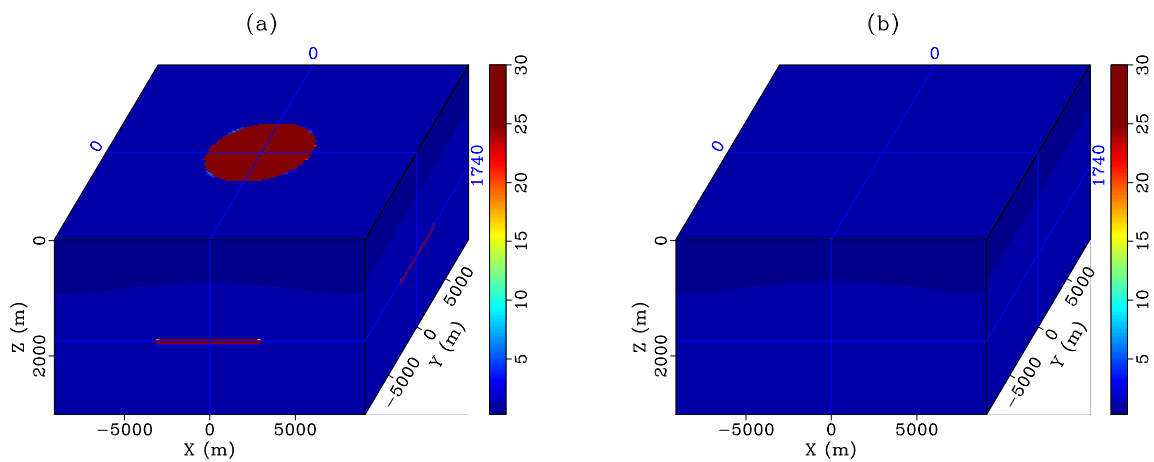


Figure 8: (a) The true resistivity model; (b) The initial resistivity model. The models are clipped at 25 Ω m for display purpose.

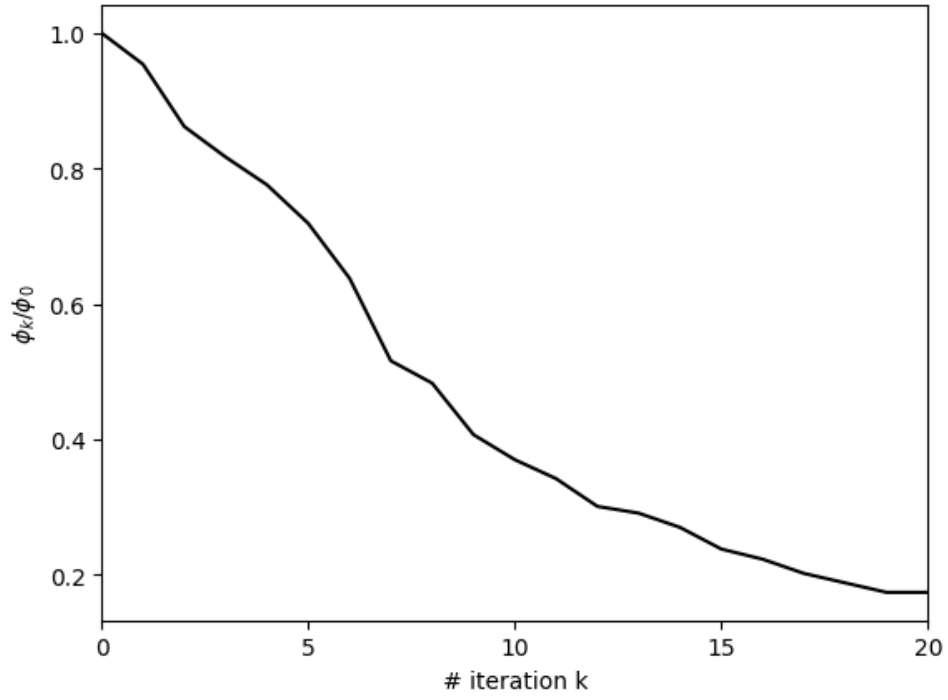


Figure 9: The convergence history of the normalized misfit for marine CSEM inversion.

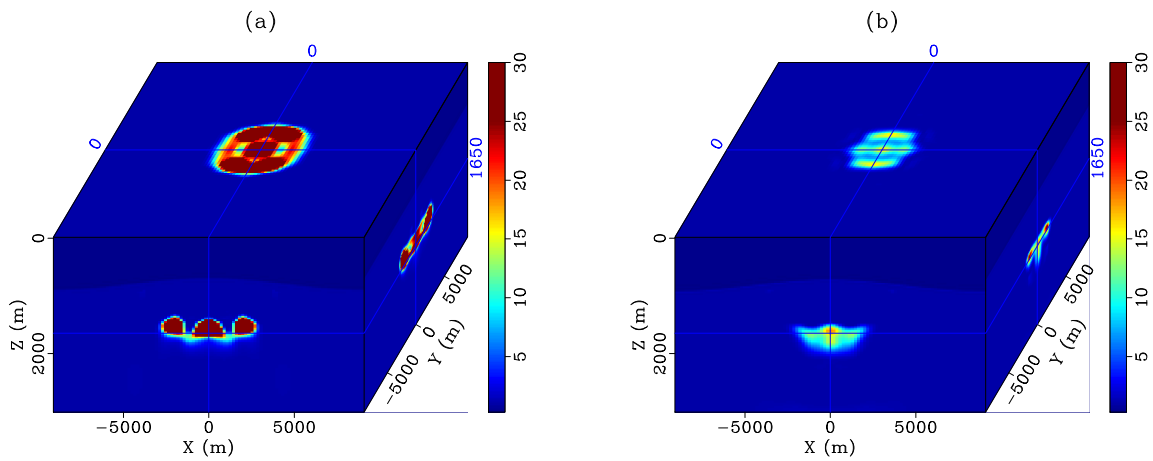


Figure 10: The result of 3D marine CSEM inversion: (a) vertical resistivity ρ_v and (b) horizontal resistivity ρ_h .

5 Discussion

It should be noted that the time series generated by our method only allows the matching of the field at given frequencies. The above inversion examples simply demonstrate that the proposed method works well, making fictitious wave domain an attractive modelling engine for 3D practical inversion. However, one has to be aware that the choice of regularization parameters β , α_x , α_y , α_z are of paramount importance to the final inversion result. Our choices may be far from perfect, and better choices should be possible to significantly improve the inversion result, while avoiding the false positives in imaging. Adding certain amount of noise for better testing and validation is also possible. These are, however, irrelevant to the key contribution of this work.

The spirit of this method is to perform frequency domain inversion using time domain modelling engine, similar to Sirgue et al. (2010) for seismic full waveform inversion (FWI). However, there are a number of differences. Switching between time and frequency domain is straightforward in seismic FWI using the definition of discrete inverse Fourier transform. One can convert frequency domain data residual using the definition of inverse discrete Fourier transform

$$s(t) = \frac{1}{2\pi} \int_{-\infty}^{\infty} s(\omega) e^{i\omega t} d\omega \approx \sum_{f=1}^{N_\omega} s(\omega_m) e^{i\omega_m t}. \quad (20)$$

Of course, the same issue presented in Sirgue et al. (2010) approach: only limited number of frequencies are available to reconstruct a long time series. The last equality in (20) assumes all the absent frequencies are zeros. Since Fourier basis is orthonormal, the computation of adjoint source time function under this assumption leads to a minimum energy solution equivalent to solving the following least-squares minimization problem

$$\min_{s(t)} \sum_m \left\| s(\omega_m) - \sum_{j=1}^{N_t} s(t_j) e^{i\omega_m t_j} \right\|^2. \quad (21)$$

Based on Parseval-Plancherel's theorem, FWI gradient can be built in frequency or in time domain via

$$\nabla \phi_d^{FWI} = \int_{\infty}^{\infty} d\omega \mathbf{v}(\mathbf{x}, \omega)^T \frac{\partial \mathbf{A}(m)}{\partial m} \mathbf{u}(\mathbf{x}, \omega) = \int_{\infty}^{\infty} dt \mathbf{v}(\mathbf{x}, t)^T \frac{\partial \mathbf{A}(m)}{\partial m} \mathbf{u}(\mathbf{x}, t), \quad (22)$$

where $\phi_d^{FWI}(m)$ is the FWI data misfit, while \mathbf{u} and \mathbf{v} are seismic forward and adjoint fields.

Note our frequency is complex-valued $\omega' = (1 + i)\sqrt{\omega\omega_0}$. Plugging the complex-valued frequency into exponential factor yields an exponentially decay factor

$$e^{i\omega' t} = e^{i(1+i)\sqrt{\omega\omega_0} t} = e^{-\sqrt{\omega\omega_0} t} e^{i\sqrt{\omega\omega_0} t}, \quad (23)$$

leaving the converted EM field possessing strong attenuation behavior, while making the basis no more orthogonal. It prohibits building the gradient directly by integrating in fictitious time domain (i.e., using the 2nd equality in equation (22) is not possible for CSEM inversion with fictitious wave modelling). This is exactly the challenge posed by fictitious wave domain approach, and why the work was carried out. A matrix-free iterative solution of adjoint source time function is evidently desirable, since direct use of inverse Fourier transform does not apply.

6 Conclusion

A nonlinear CSEM inversion based on fictitious wave domain modelling using time stepping simulation has been presented. To construct the gradient using forward and adjoint fields, the adjoint source time functions are estimated by solving a regularized linear inverse problem. An implementation using the basis functions is proposed such that the linear inverse problem can be solved once and then the resulting basis functions can be reused to build up all adjoint source time functions at every receiver location. The method enables efficient 3D CSEM inversion which are demonstrated by numerical examples. The method will become more attractive for land CSEM which normally requires much more number of frequencies than marine CSEM. The proposed method can equally be applied to magnetotelluric (MT) inversion to decipher the subsurface structure in even larger scale using much lower frequencies of the EM recordings.

Appendix: Derivation of gradient expressions

Following the adjoint state method (Plessix, 2006), the Lagrangian of the misfit functional is then constructed by adding the misfit functional with the inner product between the Lagrangian multiplier and the equality

constraint (i.e. the Maxwell equation)

$$\mathcal{L}(m, \mathbf{u}, \mathbf{v}) := \frac{1}{2} \|\mathbf{W}(\mathbf{d} - \mathbf{R}\mathbf{u})\|^2 + \Re\langle \mathbf{v}, \mathbf{A}(m)\mathbf{u} - \mathbf{f} \rangle_{\Omega \times X}, \quad (24)$$

where \mathbf{v} is the Lagrangian multiplier; \Re takes the real part of a complex number since the EM fields in the frequency domain are complex valued; the Lagrangian term has been equipped with the inner product

$$\langle \mathbf{h}, \mathbf{g} \rangle_{\Omega \times X} := \sum_{\omega} \int_X d\mathbf{x} \mathbf{h}(\mathbf{x}, \omega)^{\dagger} \mathbf{g}(\mathbf{x}, \omega) = \sum_{\omega} \int_X d\mathbf{x} \overline{\mathbf{h}(\mathbf{x}, \omega)}^{\text{T}} \mathbf{g}(\mathbf{x}, \omega), \quad \omega \in \Omega; x \in X \quad (25)$$

where $\mathbf{h} := \mathbf{h}(\mathbf{x}, \omega)$ and $\mathbf{g} := \mathbf{g}(\mathbf{x}, \omega)$ are functions defined over $\Omega \times X$; the overline takes the conjugate of the variable; \dagger stands for complex-conjugate transpose, which will degenerate to transpose $^{\text{T}}$ for real vectors and real matrices.

According to the chain rule, the gradient of the Lagrangian with respect to model parameter is then

$$\frac{\partial \mathcal{L}}{\partial m} = \frac{\partial \mathcal{L}}{\partial \mathbf{u}} \cdot \frac{\partial \mathbf{u}}{\partial m} + \frac{\partial \mathcal{L}}{\partial \mathbf{v}} \cdot \frac{\partial \mathbf{v}}{\partial m} + \Re\langle \mathbf{v}, \frac{\partial \mathbf{A}}{\partial m} \mathbf{u} \rangle_{\Omega}. \quad (26)$$

Zeroing the derivative of \mathcal{L} with respect to Lagrangian multiplier \mathbf{v} gives the forward equation in equation (6). The vector field \mathbf{u} is referred to as the forward state variable. Zeroing the derivative of \mathcal{L} with respect to the state variable \mathbf{u} yields the adjoint equation:

$$\mathbf{A}^{\dagger}(m)\mathbf{v} = \mathbf{R}^{\text{T}}\mathbf{W}^{\text{T}}\mathbf{W}(\mathbf{d} - \mathbf{R}\mathbf{u}), \quad (27)$$

where the Lagrangian multiplier \mathbf{v} is also known as the adjoint state variable (or co-state variable in optimal control theory). This shows that \mathbf{v} satisfies another Maxwell equation based on adjoint Maxwell operator $\mathbf{A}^{\dagger}(m)$. The right hand side of the adjoint equation acts as the virtual source to emanate the adjoint field.

At saddle points, both the forward equation and the adjoint equation are satisfied, thus the first two terms in equation (26) vanish ($\partial \mathcal{L} / \partial \mathbf{v} = \partial \mathcal{L} / \partial \mathbf{u} = 0$). The gradient of the misfit functional with respect to the model parameter is therefore given by the gradient of the Lagrangian

$$\frac{\partial \phi_d}{\partial m} = \frac{\partial \mathcal{L}}{\partial m} = \Re\langle \mathbf{v}, \frac{\partial \mathbf{A}(m)}{\partial m} \mathbf{u} \rangle_{\Omega}, \quad (28)$$

which is a generic expression applicable in fully anisotropic medium for the model parameters $m \in \{\sigma_{ij}, \mu\}$. Let us point out that the above gradient expression may be scaled with the local cell volume $\Delta V(\mathbf{x})$ due to the discretization of the spatial integral $\int_X d\mathbf{x}$.

References

- Abubakar, A., Habashy, T., Druskin, V., Knizhnerman, L., and Alumbaugh, D. (2008). 2.5 D forward and inverse modeling for interpreting low-frequency electromagnetic measurements. *Geophysics*, 73(4):F165–F177.
- Alumbaugh, D. and Newman, G. (1997). Three-dimensional massively parallel electromagnetic inversion-II. Analysis of a crosswell electromagnetic experiment. *Geophysical Journal International*, 128(2):355–363.
- Björck, Å. (1996). *Numerical methods for least squares problems*. SIAM, Society for Industrial and Applied Mathematics, Philadelphia.
- Chang-Chun, Y., Xiu-Yan, R., Yun-He, L., Yan-Fu, Q., Chang-Kai, Q., and Jing, C. (2015). Review on airborne electromagnetic inverse theory and applications. *Geophysics*, 80(4):W17–W31.
- Chave, A. D. and Cox, C. S. (1982). Controlled Electromagnetic Sources for Measuring Electrical Conductivity Beneath the Oceans 1. Forward Problem and Model Study. *Journal of Geophysical Research*, 87:5327–5338.
- Claerbout, J. F. and Fomel, S. (2008). *Image estimation by example: geophysical soundings image construction: multidimensional autoregression*. Stanford University.
- Commer, M. and Newman, G. A. (2008). New advances in three-dimensional controlled-source electromagnetic inversion. *Geophysical Journal International*, 172(2):513–535.
- Constable, S. (2010). Ten years of marine CSEM for hydrocarbon exploration. *Geophysics*, 75(5):75A67–75A81.

- Constable, S. and Srnka, L. J. (2007). An introduction to marine controlled-source electromagnetic methods for hydrocarbon exploration. *Geophysics*, 72(2):WA3–WA12.
- Constable, S. C., Cox, C. S., and Chave, A. D. (1986). Offshore electro-magnetic surveying techniques. In *56th Annual International Meeting, SEG, Expanded Abstracts*, pages 81–82. Society of Exploration Geophysicists.
- Constable, S. C., Parker, R. L., and Constable, C. G. (1987). Occam’s inversion: A practical algorithm for generating smooth models from electromagnetic sounding data. *Geophysics*, 52(3):289–300.
- da Silva, N. V., Morgan, J. V., MacGregor, L., and Warner, M. (2012). A finite element multifrontal method for 3D CSEM modeling in the frequency domain. *Geophysics*, 77(2):E101–E115.
- Eidesmo, T., Ellingsrud, S., MacGregor, L., Constable, S., Sinha, M., Johansen, S., Kong, F., and Westerdahl, H. (2002). Sea bed logging (SBL), a new method for remote and direct identification of hydrocarbon filled layers in deepwater areas. *First break*, 20(3).
- Ellingsrud, S., Eidesmo, T., Johansen, S., Sinha, M., MacGregor, L., and Constable, S. (2002). Remote sensing of hydrocarbon layers by seabed logging (SBL): Results from a cruise offshore Angola. *The Leading Edge*, 21(10):972–982.
- Grayver, A. V., Streich, R., and Ritter, O. (2013). Three-dimensional parallel distributed inversion of CSEM data using a direct forward solver. *Geophysical Journal International*, 193(3):1432–1446.
- Grayver, A. V., Streich, R., and Ritter, O. (2014). 3D inversion and resolution analysis of land-based CSEM data from the Ketzin CO₂ storage formation. *Geophysics*, 79(2):E101–E114.
- Gribenko, A. and Zhdanov, M. (2007). Rigorous 3D inversion of marine CSEM data based on the integral equation method. *Geophysics*, 72(2):WA73–WA84.
- Key, K. (2016). MARE2DEM: a 2-D inversion code for controlled-source electromagnetic and magnetotelluric data. *Geophysical Journal International*, 207(1):571–588.
- Lee, K. H., Liu, G., and Morrison, H. (1989). A new approach to modeling the electromagnetic response of conductive media. *Geophysics*, 54(9):1180–1192.
- Li, Y. and Key, K. (2007). 2D marine controlled-source electromagnetic modeling: Part 1—an adaptive finite-element algorithm. *Geophysics*, 72(2):WA51–WA62.
- Maaø, F. (2007). Fast finite-difference time-domain modeling for marine subsurface electromagnetic problems. *Geophysics*, 72:A19–A23.
- MacGregor, L., Barker, N., Overton, A., Moody, S., and Bodecott, D. (2007). Derisking exploration prospects using integrated seismic and electromagnetic data—A Falkland Islands case study. *The Leading Edge*, 26(3):356–359.
- MacGregor, L. and Tomlinson, J. (2014). Marine controlled-source electromagnetic methods in the hydrocarbon industry: A tutorial on method and practice. *Interpretation*, 2(3):SH13–SH32.
- Mittet, R. (2010). High-order finite-difference simulations of marine CSEM surveys using a correspondence principle for wave and diffusion fields. *Geophysics*, 75(1):F33–F50.
- Mittet, R. and Morten, J. P. (2012). Detection and imaging sensitivity of the marine CSEM method. *Geophysics*, 77(6):E411–E425.
- Morten, J. P., Bjørke, A. K., and Støren, T. (2009). CSEM data uncertainty analysis for 3D inversion. In *SEG Technical Program Expanded Abstracts 2009*, pages 724–728. Society of Exploration Geophysicists.
- Mulder, W. (2006). A multigrid solver for 3D electromagnetic diffusion. *Geophysical prospecting*, 54(5):633–649.
- Newman, G. A. and Alumbaugh, D. L. (1995). Frequency-domain modelling of airborne electromagnetic responses using staggered finite differences. *Geophysical Prospecting*, 43(8):1021–1042.
- Nocedal, J. and Wright, S. J. (2006). *Numerical Optimization*. Springer, 2nd edition.
- Oristaglio, M. L. and Hohmann, G. W. (1984). Diffusion of electromagnetic fields into a two-dimensional earth: A finite-difference approach. *Geophysics*, 49(7):870–894.

- Paige, C. C. and Saunders, M. A. (1982). ALGORITHM 583 LSQR : Sparse linear equations and least squares problems. *ACM Transactions on Mathematical Software*, 8(2):195–209.
- Plessix, R. E. (2006). A review of the adjoint-state method for computing the gradient of a functional with geophysical applications. *Geophysical Journal International*, 167(2):495–503.
- Plessix, R. E. and Mulder, W. A. (2008). Resistivity imaging with controlled-source electromagnetic data: depth and data weighting. *Inverse Problems*, 24:034012.
- Puzyrev, V., Koldan, J., de la Puente, J., Houzeaux, G., Vázquez, M., and Cela, J. M. (2013). A parallel finite-element method for three-dimensional controlled-source electromagnetic forward modelling. *Geophysical Journal International*, 193(2):678–693.
- Rochlitz, R., Skibbe, N., and Günther, T. (2019). cusem: Customizable finite-element simulation of complex controlled-source electromagnetic data. *Geophysics*, 84(2):F17–F33.
- Saad, Y. (2003). *Iterative Methods for Sparse Linear Systems*. SIAM, Philadelphia.
- Schwarzbach, C. and Haber, E. (2013). Finite element based inversion for time-harmonic electromagnetic problems. *Geophysical Journal International*, 193(2):615–634.
- Shantsev, D. V., Nerland, E. A., and Gelius, L.-J. (2020). Time-lapse CSEM: how important is survey repeatability? *Geophysical Journal International*, 223(3):2133–2147.
- Sirgue, L., Etgen, J. T., Albertin, U., and Brandsberg-Dahl, S. (2010). System and method for 3D frequency domain waveform inversion based on 3D time-domain forward modeling. US Patent 7,725,266.
- Smith, J. T. (1996a). Conservative modeling of 3-D electromagnetic fields, Part i: Properties and error analysis. *Geophysics*, 61(5):1308–1318.
- Smith, J. T. (1996b). Conservative modeling of 3-D electromagnetic fields, Part II: Biconjugate gradient solution and an accelerator. *Geophysics*, 61(5):1319–1324.
- Støren, T., Zach, J. J., and Maaø, F. A. (2008). Gradient calculations for 3D inversion of CSEM data using a fast finite-difference time-domain modelling code. In *70th EAGE Conference and Exhibition incorporating SPE EUROPEC 2008*.
- Streich, R. (2009). 3D finite-difference frequency-domain modeling of controlled-source electromagnetic data: Direct solution and optimization for high accuracy. *Geophysics*, 74(5):F95–F105.
- Taflove, A. and Hagness, S. C. (2005). *Computational Electrodynamics: The Finite-Difference Time-Domain Method*. Artech House, 3rd edition.
- Wang, T. and Hohmann, G. W. (1993). A finite-difference, time-domain solution for three-dimensional electromagnetic modeling. *Geophysics*, 58(6):797–809.
- Ward, S. H. and Hohmann, G. W. (1988). Electromagnetic theory for geophysical applications. In *Electromagnetic Methods in Applied Geophysics: Volume 1, Theory*, pages 130–311. Society of Exploration Geophysicists.
- Yang, P. and Mittet, R. (2022). Controlled-source electromagnetics modelling using high order finite-difference time-domain method on a nonuniform grid. *Geophysics*, revised.
- Zaslavsky, M., Druskin, V., Abubakar, A., Habashy, T., and Simoncini, V. (2013). Large-scale gauss-newton inversion of transient csem data using the model order reduction framework. *Geophysics*, 78(4):E161–E171.
- Zhdanov, M. S. and Keller, G. V. (1994). *The geoelectrical methods in geophysical exploration*, volume 31.